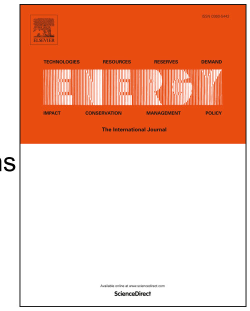


# Inventory control assessment for small scale $sCO_2$ heat to power conversion systems

Matteo Marchionni, Muhammad Usman, Lei Chai, Savvas A. Tassou

PII: S0360-5442(22)03424-7

DOI: https://doi.org/10.1016/j.energy.2022.126537

Reference: EGY 126537

To appear in: *Energy*

Received Date: 1 March 2022

Revised Date: 5 November 2022

Accepted Date: 22 December 2022

Please cite this article as: Marchionni M, Usman M, Chai L, Tassou SA, Inventory control assessment for small scale $sCO_2$ heat to power conversion systems, *Energy* (2023), doi: https://doi.org/10.1016/j.energy.2022.126537.

# Inventory control assessment for small scale $sCO_2$ heat to power conversion systems

Matteo Marchionni*, Muhammad Usman, Lei Chai, Savvas A. Tassou

Brunel University London, Institute of Energy Futures,
Center for Sustainable Energy Use in Food Chains, Uxbridge, Middlesex UB8 3PH, UK

*corresponding author: matteo.marchionni2@brunel.ac.uk

## Highlights

- Development of inventory system model considering finite capacity tanks
- Effects of inventory tanks main parameters on power block performance
- Design and analysis of Inventory PI controller
- Inventory control able to optimise system performance at part-load conditions

**Keywords**
Supercritical $CO_2$ power cycles; waste heat recovery; inventory control; transient analysis; $sCO_2$ power cycle controls; control design

**Abstract**

The control of the main cycle parameters in supercritical $CO_2$ ($sCO_2$) systems during off-design and transient operation is crucial for advancing their technological readiness level. In smaller scale power units (<0.5-5 MW), costs and complexity constraints limit the number of auxiliary components in the power loop, making the design of the control system even more challenging.

Among the possible strategies, the regulation of system inventory, which consists in varying the $CO_2$ fluid mass in the power loop to achieve a given control target, represents a promising alternative. Such technique however poses several technical challenges that are still to be fully understood. To fill this gap, this work presents a comprehensive steady-state and transient analysis of inventory control systems, referring in particular to a 50 kW $sCO_2$ test facility being commissioned at Brunel University.

Stability implications (e.g. pressure gradients in the loop) and the effects of variable inventory tank size are discussed. Tank volumes 3 times higher than the one of the power loop (including the receiver) can lead to a higher controllability range (±30% of the nominal turbine inlet temperature) and an extended availability of the control action (slower tank discharge). A PI controller is also designed to regulate the turbine inlet temperature around the target of 465°C in response to waste heat variations.

**Nomenclature:**

*Symbols:*

| | | |
|---|---|---|
| $\xi$ | Pressure loss coefficient | [-] |
| $\rho$ | Density | [kg/m$^3$] |
| $\sigma$ | Surface tension | [Pa] |
| $\upsilon$ | Dynamic viscosity | [m$^2$/s] |
| $dx$ | Displacement | [m] |
| $f$ | Fanning friction factor | [-] |
| $h$ | Heat transfer coefficient | [W/(m$^2$K)] |
| $m$ | Mass | [kg] |
| $\dot{m}$ | Mass flow rate | [kg/s] |
| $p$ | Pressure | [bar] |
| $t$ | Time | [s] |
| $v$ | Velocity | [m/s] |
| $A$ | Area | [m$^2$] |
| $C_1$ | Pressure drop calibration coefficient | [-] |
| $C_d$ | Discharge coefficient | [-] |
| $D$ | Diameter | [m] |
| $H$ | Specific enthalpy | [kJ/kg] |
| $L$ | Length | [m] |
| $Nu$ | Nusselt number | [-] |
| $Pr$ | Prandtl number | [-] |
| $R$ | Radius | [m] |
| Ra | Surface roughness | [µm] |
| $Re$ | Reynolds number | [-] |
| $T$ | Temperature | [°C] |

*subscripts:*

| | |
|---|---|
| $b$ | bubble |
| $wl$ | wall |
| $wf$ | working fluid |
| $0$ | total |
| $\infty$ | boundaries |

*Acronyms:*

| | |
|---|---|
| CBV | Compressor By-pass Valve |
| CGT | Compressor-Generator-Turbine |
| EXTV | Inventory Extraction Valve |
| GWP | Global Warming Potential |
| HP | High Pressure |
| INJV | Inventory Injection Valve |
| LP | Low Pressure |
| ODP | Ozone Depletion Potential |
| PCHE | Printed Circuit Heat Exchanger |
| PHE | Plate Heat Exchanger |
| PHX | Primary heat exchanger |
| PI | Proportional-Integral |
| $sCO_2$ | Supercritical carbon dioxide |
| SS 316L | Stainless steel 316L |
| TBV | Turbine By-pass Valve |
| WHR | Waste Heat Recovery |

## 1. Introduction

Recently, power cycles with carbon dioxide in the supercritical state ($sCO_2$) as the working fluid have received a strong interest by academia and industry [1]. Compared to state-of-the-art technologies such as steam and organic Rankine systems, $sCO_2$ systems have the following advantages: global conversion efficiency up to 10% higher (compared to other technologies) thanks to reduced compression work near the critical point (33.0 °C, 74bar); better heat utilisation (exergy efficiency) due to absence of phase change during the heat recovery process; less cycle temperature limitations; higher power flexibility, along with smaller footprint, better water utilisation and higher thermal stability. Furthermore, $CO_2$ is an environmentally friendly working fluid, having unitary Global Warming Potential (GWP) and zero Ozone Depletion Potential (ODP).

The interest in $sCO_2$ technology goes beyond high temperature waste heat to power conversion [2] and covers the whole spectrum of power generation, from fossil fuel to nuclear and renewable applications. The high efficiency potential and extremely compact turbomachinery make it also an attractive alternative propulsion technology [3].

Research on $sCO_2$ power systems is currently focused on thermodynamic and techno-economic analyses to identify the optimal cycle layouts both using pure $CO_2$ or blends (mixtures of $CO_2$ and other fluids, often called dopants [4]) with additional focus areas related to investigations of performance at component level, i.e. turbomachinery and heat exchangers as well as at fundamental scale, i.e. flow topology in converging-diverging nozzles or heat transfer [1].

Studies on off-design and transient operating regimes of $sCO_2$ power systems are limited due to low availability of experimental datasets from the small pool of test facilities whose total world count is below 15 [2]. These reasons also reflect the scarce literature on the control of $sCO_2$ power cycles. In general, the $sCO_2$ control narratives are derived from closed loop Brayton cycle experiences with helium or argon [5]. However, the highly non-ideal nature of $sCO_2$ differentiates it from from other Brayton cycles and introduces additional control considerations close to the critical point. For this reason, the majority of the works are focused on regulating the inlet conditions of the compressor and turbine to ensure the optimal and stable operation of the system.

Deviation in inlet density conditions can cause significant changes to flow conditions in the compressor leading to overall cycle performance and controllability issues. To operate the compressor in an optimal and safe operating region, different methods have been proposed, such as regulation of the heat sink conditions [6] or the action on the flow split ratio between compressor and recompressor [7]. For the turbine, the use of throttling or by-pass valves is being considered [8,9].

Alongside turbomachinery bypass and throttling, inventory control is a key strategy to modulate the power output of $sCO_2$ power systems to enhance their flexibility [9], i.e. their ability to promptly and efficiently adapt to variations in operating conditions imposed by the heat source (e.g. industrial manufacturing process), the heat sink (environmental factors) or the grid (demand variability, volatility of renewable energy sources in the power mix).

Such advantages have been demonstrated by [9,10], whose research concerned the development of mixed control strategies involving a conjunct use of by-pass, throttling and inventory control to follow the generator load of a

$sCO_2$ recompression power unit for nuclear applications. The author in [11] presented different inventory control schemes and compared them in terms of response time and effectiveness. This included the adoption of a single inventory tank connected to both the low- and high-pressure side of the circuit or the use of multiple tanks connected to different charging/discharging points. However, stability implications (e.g. pressure gradients in the loop) due to the withdrawals/additions of $CO_2$ and the implications of having finite storage capacity in the inventory storage tanks have not been adequately considered in the literature.

To fill the literature gap, this research advances the state of the art through a numerical assessment of the effects of inventory control on the dynamic response of a small-scale $sCO_2$ heat to power system. A unique feature of this study is the modelling methodology that combines the dynamics of the $sCO_2$ heat to power unit (calibrated against real equipment data) with those of the inventory control system using finite capacity tanks. Insights on the dynamic behaviour of the inventory system to support the design and thermal management of the $CO_2$ storage tanks are provided. A Proportional Integral (PI) inventory controller has been designed to regulate the turbine inlet temperature following variations of the waste heat loads. Its response and effect on system performance and main cycle parameters are then analysed and discussed.

## 2. System description

The modelled $sCO_2$ system refers to a plug and play 50 kWe $sCO_2$ unit for Waste Heat Recovery (WHR) applications available at Brunel University London. The $sCO_2$ facility in Figure 1 is based on a simple regenerative Joule-Brayton cycle (Figure 1.a) and it is equipped with three heat exchanger technologies: a micro-tube gas/$sCO_2$ heat exchanger for direct heat recovery from the heat source; a Printed Circuit Heat Exchanger (PCHE) employed as recuperator; and a Plate Heat Exchanger (PHE) as gas cooler. PCHEs are commonly used in the oil and gas sector because of their reliability in operating at high pressures and temperatures [12],For this reason, they have also been adopted in $sCO_2$ power applications [13] as recuperators and also gas coolers [14]. For the Brunel test facility a plate heat exchanger (PHE) has been selected as gas cooler to reduce cost. TThis is of paramount importance in WHR applications.

Other components include a radial turbine, a radial compressor and a synchronous brushless generator/motor mounted on the same single shaft, and motorised compressor and turbine by-pass globe valves (CBV and TBV respectively shown in Figures 1.a and 1.c) to control the system at nominal, startup, shutdown and emergency operations. The CBV valve is located between the compressor outlet and gas cooler inlet while TBV is placed between the turbine inlet and outlet (Figure 1.c). All such components are packaged in a standard 20 ft container (Figure 1.c) except for the micro-tube heat exchanger, also known as primary heater, which is located along the exhaust line of the Process Air Heater (Figure 1.b). The Process Air Heater simulates the industrial waste heat source and provides flue gases up to 1.0 kg/s and temperatures up to 800 °C. The facility is also equipped with a 500 kW dry cooler system that rejects heat form the gas cooler to the ambient. Variable speed drives for the water pump and fans of the dry cooler allow variation of heat removal from the hgas cooler.

A data acquisition and control system has been also installed (left-hand side of Figure 1.c) to enable remote control and monitoring of the unit. Two 10-meter pipes connect the loop packaged in the container to the primary heater, which has been specifically designed to enhance the gas/$sCO_2$ heat transfer without causing an excessive pressure drop on the flue gas side. The $sCO_2$ test facility has been designed for small scale waste heat recovery applications (with an estimated net power output in the range of 50-75 kWe at design conditions). At these operating conditions, the turbomachinery impellers become very small and high speed which impacts negatively on their efficiency. Another challenge of small-scale $sCO_2$ systems is the cost per kilowatt installed. Their capital expenditure (CAPEX) is not linear with the power size especially in the case of the heat exchangers, which typically are responsible for the majority of the equipment budget [14].

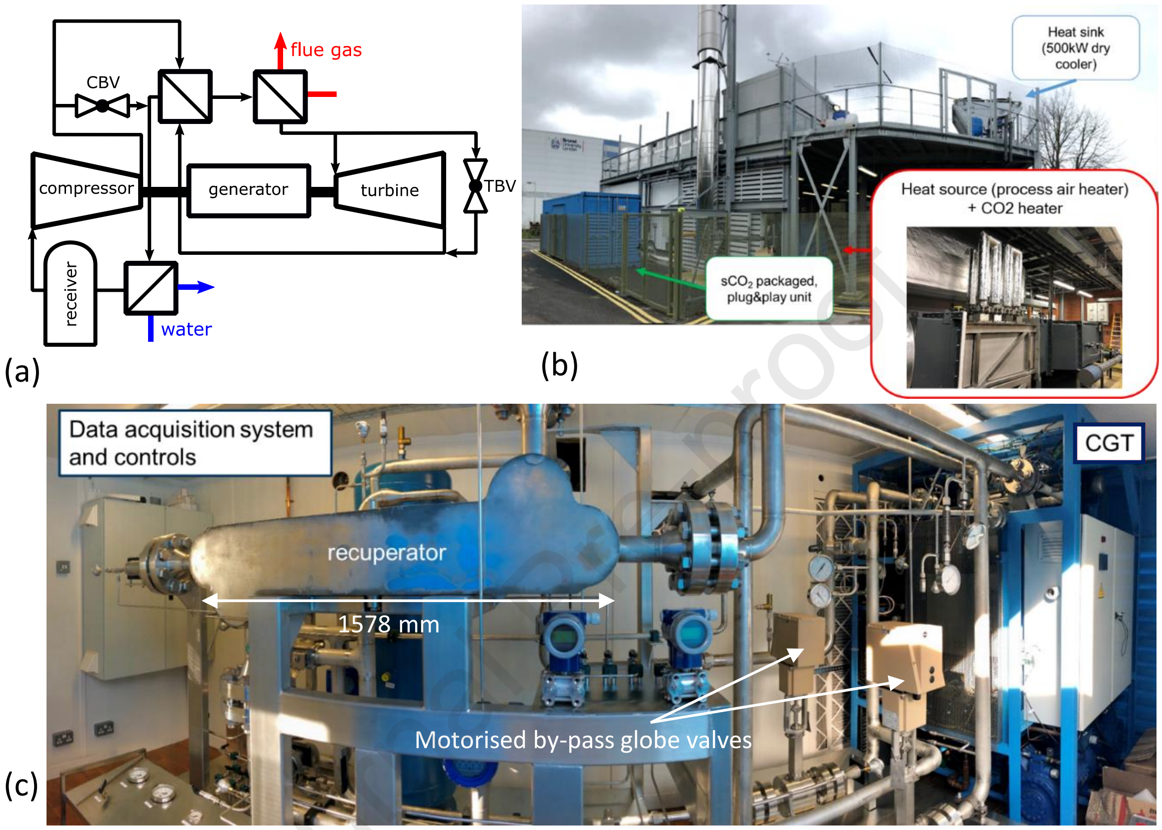


Figure 1 – $sCO_2$ facility at Brunel University London: (a) system layout, (b) facility overview, (c) $sCO_2$ loop inside the blue container shown in (b).

Unless costs are significantly reduced, $sCO_2$ technology is primarily competitive for applications beyond 1 MWe power output and heat-source temperatures above 350°C. Despite the low power output, this pilot scale research is expected to advance the knowledge in the field of $sCO_2$ power research and further support the uptake of $sCO_2$ technology. Furthermore, as reported in [17] $sCO_2$ turbomachinery will still have to be radial as long as the system power output stays below 12 MWe. For these reasons, the analysis reported in the following sections should be transposable to the design and operation of full-scale $sCO_2$ power systems. Further details on Brunel's high-temperature heat to power conversion (HT2C) facility are available in [18]. Figure 2 shows a simplified P&ID of the facility detailing in particular the location of pressure, temperature and mass flow rate sensors in the unit. Tables 1 and 2 detail the sensors installed and the estimated uncertainty of efficiencies and power for each system component..

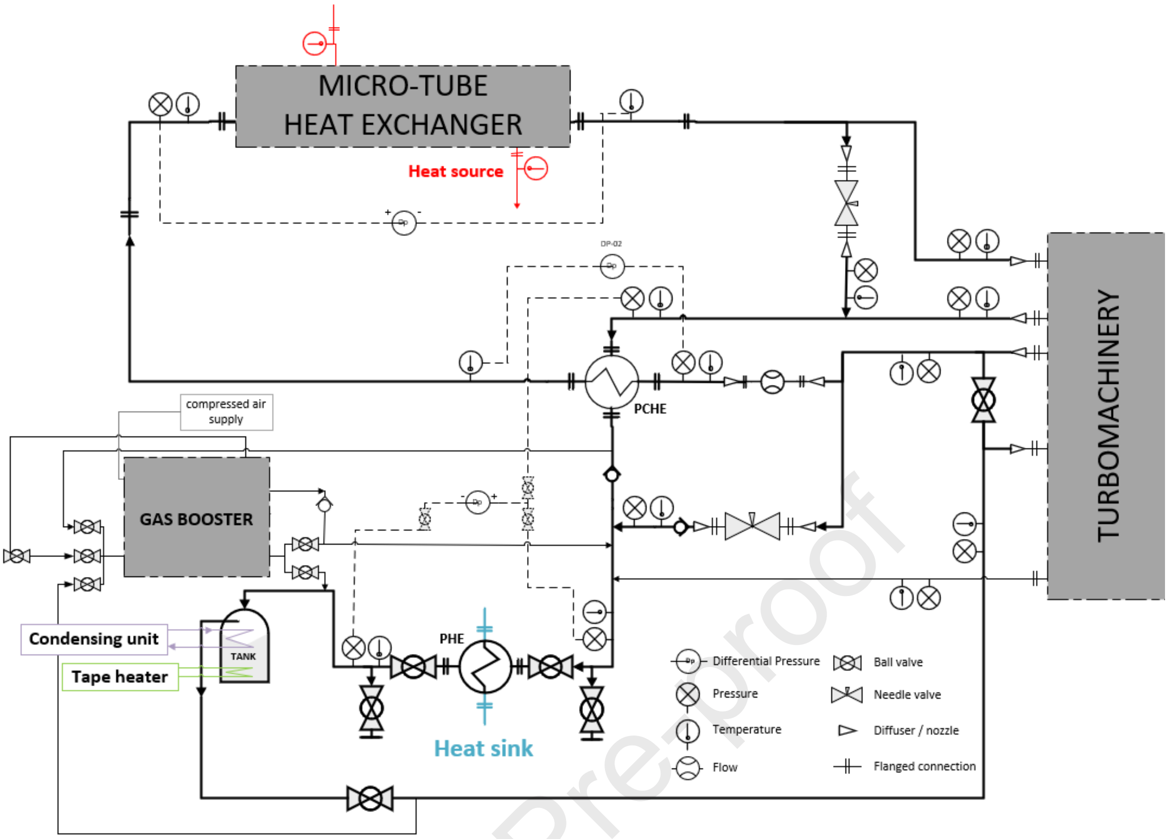


Figure 2 – Simplified P&ID of the $sCO_2$ facility at Brunel University London (Adapted from [16])

Table 1 – Summary of transducers accuracies [16].

| Accuracy | High | Standard |
|---|---|---|
| High pressure transducers | 0.17 bar | 0.52 bar |
| Low pressure transducers | 0.10 bar | 0.34 bar |
| Temperature transducers (RTD) | 0.03K | 0.06K |
| DP transducers | 1.9mbar | |
| Mass flow rate (Coriolis) | 0.35% of measured value | |

Table 2 – Estimated measurement uncertainty at design conditions [16].

| Uncertainty | Power | Efficiency |
|---|---|---|
| Compressor | 2.66% | 3.32% |
| Turbine | 0.43% | 0.47% |
| Heater | 0.36% | |
| Recuperator (cold/hot side) | 0.36%/0.35% | |
| Cooler | 0.61% | |

## 3. Modelling methodology

The model of the $sCO_2$ heat to power conversion system has been developed in the commercial software GT-SUITE™. This tool is based on a one-dimensional (1D) formulation of Navier-Stokes equations and on a staggered grid spatial discretization [19]. Each component can be independently modelled through input data relating to geometrical features as well as their performance.

The components modelled as equivalent 1D objects are heat exchangers and pipes while the turbomachines, valves and the receiver are treated with a lumped approach. The 1D models discretise the components into a series of capacities such that manifolds are represented by single volumes while pipes are divided into one or more volumes. These volumes are connected by boundaries. The scalar variables (pressure, temperature, density, internal energy, enthalpy, etc.) are assumed to be uniform in each volume. On the other hand, vector variables (mass flux, velocity, mass fraction fluxes, etc.) are calculated for each boundary [19]. Each capacity considers the algebraic sum of all the incoming and outgoing mass flow rate contributions occurring at the boundaries (B), as per the continuity equation (1).

$$\frac{dm}{dt} = \sum_{i=1}^{B} \dot{m}_i \tag{1}$$

The pressure dynamics in the system is calculated through the momentum equation (2), which neglects body forces and considers the algebraic sum of momentums through the boundaries, pressure forces and dissipations due to friction and pressure drops [19]. In pipes, the latter two terms are respectively related to distributed (i.e. due to surface roughness) or concentrated (i.e. due to bends) pressure losses.

$$\frac{d(\dot{m}v)}{dt} = \frac{1}{dx}\left( dpA + \sum_{i=1}^{B} (\dot{m}v)_i - 4f\,\frac{\rho v|v|}{2}\frac{dxA}{D} - \xi\left(\frac{\rho v|v|}{2}\right)A \right) \tag{2}$$

The energy equation (3) is expressed in terms of total enthalpy. This formulation is required for the further implicit integration scheme employed by the solver for the analysis of energy systems whereas resolving fast dynamics (e.g. indicating pressure in positive displacement machines) is not the end goal [19]. Neglecting variations of potential energy, for a given capacity, the rate of change of total enthalpy depends on the volume capacity variations, the enthalpy fluxes and the heat transfer phenomena. The solution of the energy equation requires the computation of the local heat transfer coefficient through calibrated heat transfer correlations.

$$\frac{d(\rho H_0 V)}{dt} = \sum_{i=1}^{B} (\dot{m}H_0)_i + V\frac{dp}{dt} - hA\left(T_{wf} - T_{wl}\right) \tag{3}$$

### *3.1. Heat exchangers*

The properties of the equivalent 1D channels of heat exchangers are defined starting from the geometrical inputs of the component. The performance data, which refer to different operating conditions of the heat exchangers, are used to compute the best fitting coefficients of the Nusselt-Reynolds (Nu-Re) correlations along the equivalent 1D networks [19]. Such data are provided by the manufacturers or calculated from more complex models (e.g. 3D CFD).

Table 3 summarises the geometrical features of the PCHE recuperator as well as the number of sub-volumes in which the different heat exchangers have been discretized. Their time constants have been also reported, calculated as the ratio between the heat exchanger mass multiplied by the specific heat capacity (*m*cp*) of the material and conductance (UA) of the heat exchanger. It can be seen that the primary heater (PHX) has the lowest thermal inertia and the recuperator the highest due to its much higher thermal mass of the material used for its manufacture.

The results of the regression analyses carried out to calibrate the several heat exchangers are detailed in Table 4, which compares the Re-Nu curve interpolation of the different data provided by the manufacturer against the ones obtained by using the Gnieliski [20] and Dittus-Boelter [21] heat transfer correlations. It can be observed that the Gnieliski correlation provides better predictions of the manufacturer data. For this reason, in the absence of data on heat exchanger performance from experimental tests, the Gnieliski correlation for the calculation of the heat transfer coefficients was employed in this study [22]. The full modelling methodology is available at [22].

Table 3 – Heat exchangers specifics.

| Flow parameters | | PHX | PCHE | PHE |
|---|---|---|---|---|
| Nominal heat duty | kW | 388.3 | 630.0 | 237.5 |
| Nominal UA value | kW/K | 1.3 | 20.3 | 16.8 |
| Hot side pressure drop | kPa | 1.1 | 128.0 | 8.7 |
| Cold side pressure drop | kPa | 64.0 | 120.0 | 89.1 |
| Geometrical features | | | | |
| Heat transfer surface | $m^2$ | 3.92 | 12.00 | 6.21 |
| Hydraulic diameter | mm | 2.00 | 1.22 | |
| Dry weight | kg | 305.0 | 305.0 | 52.4 |
| Material | - | Inconel 718 | SS 316L | |
| Model details | | HX | PCHE | PHE |
| Time constant | s | 1.55 | 7.25 | 2.38 |
| Channel sub-volumes | # | 25 | 50 | 50 |

The pressure drops are computed using a modified version of the Colebrook relationship in Equation (4). In this expression, the Fanning factor is calculated using the explicit approximation of the Colebrook equation proposed by Serghides [23], which is valid for the turbulent regime ($Re_D$>2100). The quantities C2 and C3, which can be calculated using Equations (5) and (6), account for the roughness of the heat exchanger channels Ra. The term C1 is the calibration coefficient used to adapt the simulation results to the performance data provided by the heat exchanger manufacturer.

Even though this modelling methodology is common to all the three heat exchangers considered, the gas cooler requires an additional correlation to account for possible condensation of $CO_2$. In this case, to predict the phase change, the formation of vapor bubbles or liquid droplets is addressed by evaluating the fluid density in each sub volume, while the two-phase area is computed using the vapour Rayleigh-Plesset formulation in Equation (7) [24].

$$f = C_1\left(\frac{1}{4}\left(4.781-\frac{(C_2-4.781)^2}{C_3-2C_2+4.781}\right)^{-2}\right) \tag{4}$$

$$C_2 = -2.0\log_{10}\left(\frac{Ra/D}{3.7} + \frac{12}{\mathrm{Re}_D}\right) \tag{5}$$

$$C_3 = -2.0\log_{10}\left(\frac{Ra/D}{3.7} + \frac{2.51C_2}{\mathrm{Re}_D}\right) \tag{6}$$

$$\frac{p_b - p_\infty}{\rho} = R\frac{d^2R}{dt^2} + \frac{3}{2}\left(\frac{dR}{dt}\right)^2 + \frac{4\upsilon}{R}\frac{dR}{dt} + \frac{2\sigma}{\rho R} \tag{7}$$

Table 4 - Heat exchanger calibration data (Cal) and comparison with model interpolation (Int), Gnieliski (Gn) and Dittus-Boelter (DB) correlations.

| | | Re=20000 | | Re=25000 | | Re=30000 | |
|---|---|---|---|---|---|---|---|
| | | Nu | Err% | Nu | Err% | Nu | Err% |
| Heater | Cal | 73.0 | N/A | 92.2 | N/A | 106.8 | N/A |
| | Int | 73.4 | 1.3 | 92.5 | 0.3 | 107.2 | 0.4 |
| | Gn | 75.7 | 2.7 | 90.9 | 1.4 | 101.9 | 4.8 |
| | DB | 80.1 | 8.7 | 96.5 | 4.4 | 108.6 | 1.6 |
| Recuperator | Cal | 596.2 | N/A | 767.6 | N/A | 876.9 | N/A |
| | Int | 596.2 | 0.0 | 756.8 | 1.4 | 878.1 | 0.1 |
| | Gn | 596.9 | 0.1 | 735.6 | 4.2 | 886.2 | 1.0 |
| | DB | 629.4 | 5.3 | 779.9 | 1.6 | 944.7 | 7.2 |
| Cooler | Cal | 371.5 | N/A | 464.0 | N/A | 560.1 | N/A |
| | Int | 373.4 | 0.5 | 454.6 | 2.1 | 554.5 | 1.0 |
| | Gn | 376.5 | 1.3 | 445.4 | 4.2 | 544.7 | 2.8 |
| | DB | 369.1 | 0.6 | 437.0 | 6.2 | 533.2 | 5.0 |

### *3.2. Turbomachines*

The turbomachines have been modelled as lumped components by using performance maps. The performance maps use the boundary conditions (temperature/pressure and shaft speed) to evaluate the performance of the machine and outlet conditions. The advantage of modelling the turbomachinery with performance maps is that it allows faster calculation results as the model is reduced order and also the dynamics of turbomachinery is relatively faster compared to the heat exchangers and other components with higher volume and high thermal inertia. Their aerothermal design is detailed in Table 5. Performance maps have been calculated by performing 3D RANS CFD simulations whose modelling methodology has been discussed in [26,27]. The 3D modelling approach has been validated through experimental data available from the Sandia National Laboratories [28], with an uncertainty lower than 5% [26,27]. The inlet boundary conditions of the 3D model are the total pressure and temperature as well as the flow direction, which is considered normal to the boundary. Outlet average static pressure has been chosen as outlet boundary condition.

The turbine operating and isentropic efficiency maps have been expressed through reduced quantities (pressure ratio versus reduced mass flow rates and reduced revolution speed) in order to account the variation of turbine performance on a change of the inlet conditions. Representation of turbine maps can be also found in [22].

Table 5: Summary of the turbomachinery aerothermal design.

| | Turbine | Compressor |
|---|---|---|
| Diameter | 72 mm | 55 mm |
| No. of blades (Rotor) | 14 | 7 |
| No. of blades (Nozzle) | 17 | 11 |
| Isentropic efficiency (total-to-static) | 70% | 76% |

Although this approach is fine for the turbine, which operates in a region where the $CO_2$ behaviour can be considered similar to the one of an ideal gas, this does not hold for the compressor, which operates near the fluid critical condition. Furthermore, the use of maps based on reduced quantities for the compressor leads to numerical instabilities when dealing with the inventory control action.

Therefore, the compressor map has been condensed to one curve using non-dimensional parameters, following the approach detailed in [29]. This allowed to solve numerical instabilities following the simulation of the inventory control action and to better account the effect of variable compressor inlet conditions on its performance. The inertia of the shaft has been modelled but the electrical machine characteristics have not been covered in scope of current work. The losses and consumptions of auxiliary equipment for turbomachinery lubrication and cooling have also been neglected.

*3.3. Valves and other equipment*

The valves have been modelled as orifices with variable area. A look-up table provides a series of forward and reverse discharge coefficients as a function of the lift position of the valve actuator. Such data have been retrieved by the manufacturer of the needle valves [30], which have been designed to follow an equal percentage characteristic curve. These discharge coefficients are then used to compute the effective flow area at the throat, while the pressure ratio across the valves allows to calculate the velocity at the throat. The velocity multiplied by the fluid density and the throat flow area gives then the mass flow rate passing through the valve. Equation (8) shows the correlation relating the valve discharge coefficient to the ratio between the actuator lift $L$ and the valve diameter $D$ [30].

$$C_d = 0.0112 e^{0.196\frac{L}{D}} \tag{8}$$

The 1D modelling approach used to simulate heat exchanger behaviour has been adopted as well for straight pipes and bends. Bends introduce concentrated pressure drops while pipes have been considered as smooth and insulated, which means thermal losses are neglected. This assumption is reasonable based on the relatively large value of pipe diameters used in the Brunel $sCO_2$ test facility to minimise pressure drop as well as their insulation with ceramic wool layer wrapped between an inner layer of silica wash treated glass cloth and an outer layer of grey PTFE coated glass cloth to reduce heat losses.

The receiver, situated downstream the gas cooler (Figure 2) to absorb the thermal expansion of the fluid in the circuit, has been modelled as a container (capacity) with fixed volume. Its volume is 0.165 $m^3$ and accounts for almost 50% of the overall system capacity.

### 3.4. *Inventory system*

The inventory control system considers two tanks, modelled as finite volumes, whose value can be set as inputs to the model. The arrangement of the two tanks is shown in the schematic representation of the system in Figure 3. The inventory tank connected downstream of the compressor (on the high pressure, HP, side of the circuit, point 15 in Figure 3) has always a pressure lower than the one on the discharging point on the circuit (point 2, Figure 3). Such pressure difference between the tank and the loop drives the withdrawal and storage of the working fluid from the loop to the tank respectively. The variable opening of a valve (namely the extraction valve, EXTV) allows to regulate the amount of fluid flowing from the loop to the tank. The other inventory tank connected upstream of the compressor (on the low pressure, LP, side of the circuit, point 1 in Figure 3) enables the injection of additional $CO_2$ to the loop. In this case, to drive the fluid injection from the tank to the loop, the tank pressure (point 13, Figure 3) is higher than the one at the charging point (point 1, Figure 3). Another valve (namely the injection valve, INJV) can be actuated to regulate the fluid injection into the circuit.

Both valves are modelled as orifices as detailed in the previous section. The inventory tank sub-models require as boundary conditions the tank volume, the initial tank fluid temperature and initial pressure. An initialization process starts  then, based on these three variables, the initial mass of fluid in the tanks at the beginning of the simulation (point 12 and 14, Figure 3).

Figure 3 also shows the general model boundary conditions required for the simulations, which are indicated with lower case letters. These boundary conditions are the revolution speed of the compressor-generator-turbine unit along with the inlet temperatures, pressures and mass flow rates of the hot and cold sources. The thermodynamic properties of the fluids are computed using an interface between the solver and the NIST database [31].

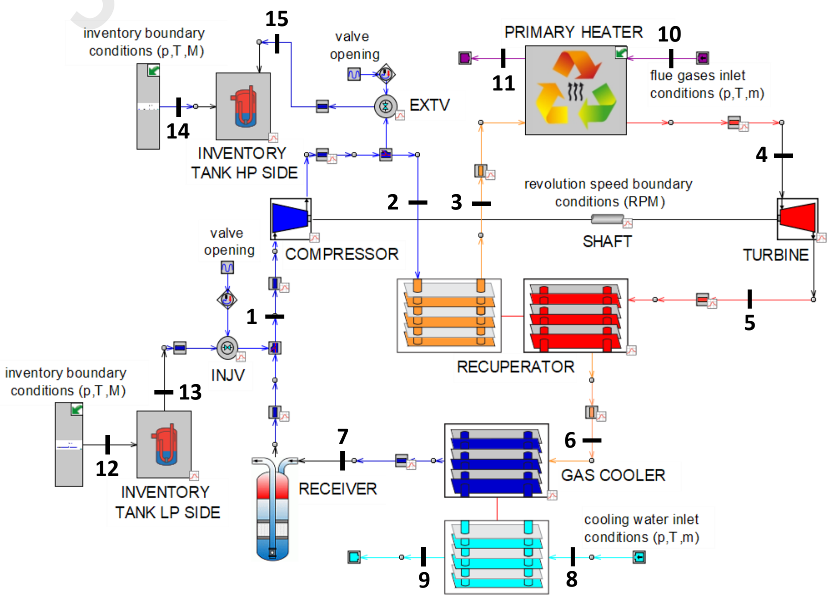


Figure 3 – Model diagram of the full $sCO_2$ heat to power conversion block including inventory system

## 4. Inventory tank assessment

To broadly assess the impact of potential inventory control actions on the main thermodynamic variables of the tanks and the loop, the injection and the withdrawal of $CO_2$ into and from the circuit has been simulated assuming different inventory tank initial pressures and volumes. For each of the simulations the inlet conditions of the heat source and sink as well as the revolution speed of the turbomachines has been kept constant and equal to the nominal values (Table 6).

A pre-defined opening profile for the EXTV and INJV valves has been set and maintained constant for all the simulations. Such opening profile has been selected considering a valve opening time required to allow the achievement of steady-state conditions in the loop and in the tanks after the $CO_2$ injection/withdrawal actions are performed.

Table 6 – Nominal operating conditions and performance of the $sCO_2$ heat to power conversion loop.

| Supercritical $CO_2$ | | Design | Model I/O |
|---|---|---|---|
| Mass flow rate | kg/s | 2.2 | Output |
| Highest pressure | bar | 137.5 | Output |
| Lowest pressure | bar | 75.0 | Output |
| Highest temperature | °C | 465 | Output |
| Lowest temperature | °C | 33 | Output |
| Heat source: flue gas | | | |
| Mass flow rate | kg/s | 1.0 | Input |
| Inlet temperature | °C | 650 | Input |
| Inlet pressure | bar | 1.0 | Input |
| Cold source: Water | | | |
| Mass flow rate | kg/s | 1.6 | Input |
| Inlet temperature | °C | 15 | Input |
| Inlet pressure | bar | 3.0 | Input |
| $sCO_2$ unit | | | |
| Net thermal power output | kW | 75 | Output |
| Overall efficiency | % | 24 | Output |
| Turbomachinery speed | RPM | 86000 | Input |
| Mass charge | kg | 61 | Input |

### 4.1. Inventory tank dynamics

Figure 4 shows the inventory tank dynamics following the injection and withdrawal of $CO_2$ in the loop assuming an inventory tank capacity equal to the one of power loop (0.243 $m^3$). Each different initial tank pressure is represented by a different line. The range of pressures analysed varies from 82.5 bar up to 112.5 bar for both inventory tanks. The initial mass and temperature levels of the $CO_2$ in the tanks are correlated to the initial pressure and tank capacity considered (Table 7) across a range between 88-152 kg and 38-45°C respectively.

Table 7 – Main simulation parameters of inventory system

| Initial conditions at both inventory tanks | | Min | Max |
|---|---|---|---|
| Pressure (Model input) | bar | 82.5 | 112.5 |
| Volume (Model input) | $m^3$ | 0.073 | 0.729 |
| Temperature (Model output) | °C | 38 | 45 |
| Mass (Model output) | kg | 88 | 152 |

Figure 4.a-c shows the pressure, temperature and mass transient profiles of the inventory tank connected to the low-pressure side of the system after the INJV valve opening. During the 50s transient, the $CO_2$ stored in the tank is injected into the loop, causing an expansion and thus cooling the gas contained in the tank. The temperature does not fall below the critical point, eliminating the risk of condensation (Figure 4.b). However, more detailed numerical simulations or experimental analyses may be required to assess local heat transfer phenomena and potential risks of blowdown, at least in the most extreme cases where the pressure of the $CO_2$ goes from 112.5 bar down to 89 bar with a resulting temperature drop of 8°C (Figures 4.b and 4.c).

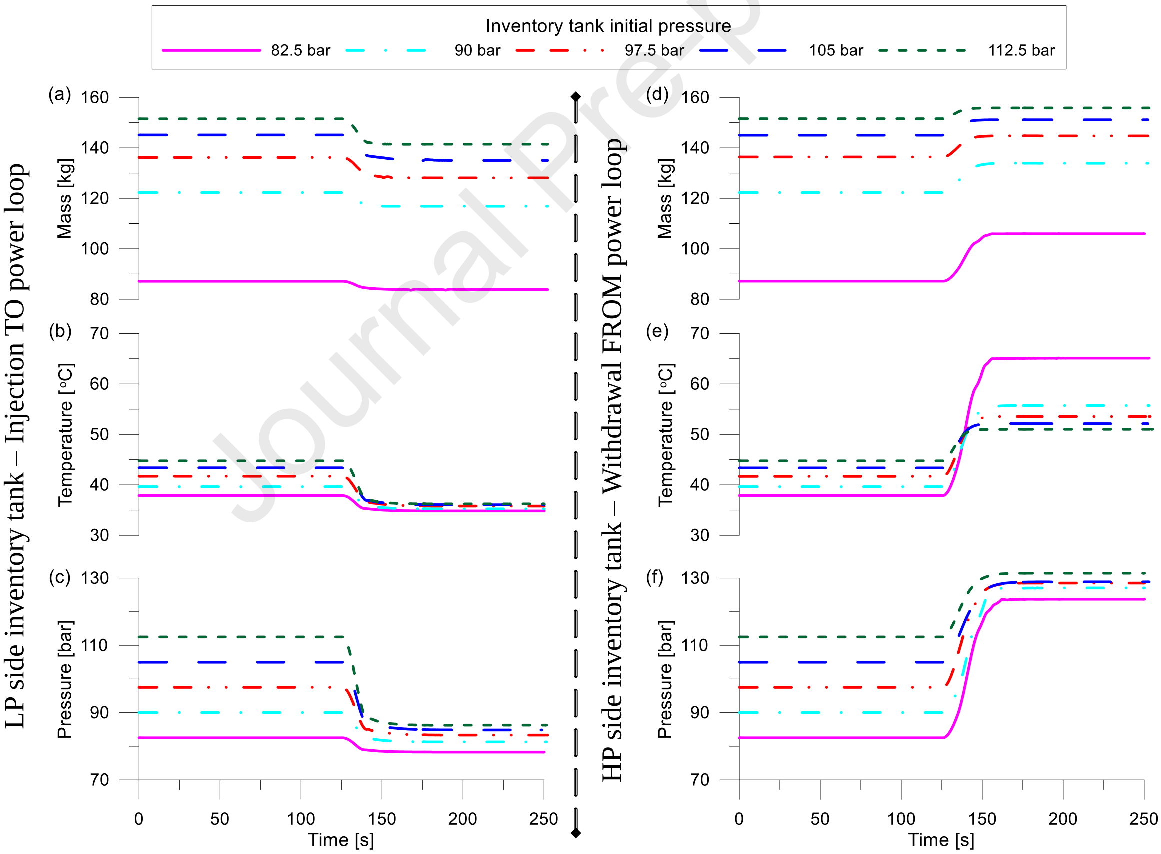


Figure 4 – Effects on tank mass (a), temperature (b) and pressure (c) following the injection of $CO_2$ into the power loop (left-hand side) or an extraction of $CO_2$ from the power loop (right-hand side) for a tank volume equal to the one of the loop

Symmetric trends can be observed during the extraction of fluid from the $CO_2$ loop to inventory tanks connected to the high-pressure side of the loop (downstream the compressor, Figure 4.d-f). The only slight difference can be noticed in the temperature profiles, where the larger temperature variation, from 38°C to 65°C, occurs when the initial pressure level of the HP side tank is set to 82.5 bar. In this case, the mass of $CO_2$ contained in the vessel is lower compared to the other cases, and therefore the stream of $CO_2$ flowing at higher temperature from downstream the compressor has a higher impact in warming up the tank (Figure 4.e).

The results also show that both the injection and withdrawal processes cannot be considered isothermal, given the relevant temperature variations occurring during the fluid expansion ($CO_2$ injection) and during the fluid compression in the tank following mixing with the higher temperature and pressure $CO_2$ stream flowing from the loop ($CO_2$ extraction). This assumption in the sizing stage of the tanks could lead to errors in the predictions of the control action outcomes, given the high dependency of the thermophysical properties of $CO_2$ on pressure and temperature changes.

Figures 4.a and 4.d show the working principle of the inventory control action. Transferring part of the mass contained in the inventory tank to the $CO_2$ circuit ($CO_2$ injection, Figure 4.a) and vice versa ($CO_2$ withdrawal, Figure 4.d), enables the mass of $CO_2$ in the circuit to be altered in order to adapt the system electric output to the grid load, but also, for a given heat load, decreasing/increasing the temperature at the turbine inlet. This effect is shown in Figure 5.

In particular, Figure 5.a shows that injection of $CO_2$ into the loop leads to a decrease in the $CO_2$ turbine inlet temperature from the nominal level of 460°C down to 414°C, 381°C, 372°C, 363°C and 350°C for a LP side inventory tank initial pressure of 82.5 bar, 90.0 bar, 97.5 bar, 105.0 bar and 112.5 bar respectively. Lower initial tank pressures lead to lower injection of $CO_2$ mass into the system and therefore to higher turbine inlet temperatures. The opposite holds for the temperature at the compressor inlet (Figure 5.a), since in the same way, higher mass in the circuit for a given cooling load leads to higher temperature at the gas cooler outlet and therefore at the compressor inlet.

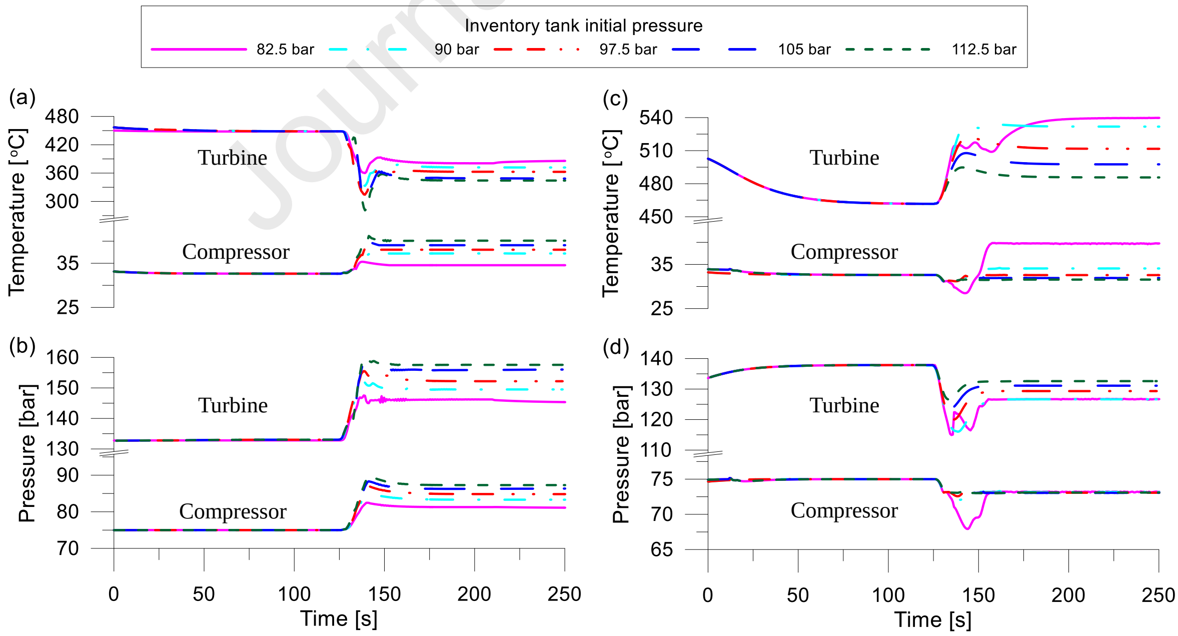


Figure 5 – Effects on compressor and turbine inlet temperature (a) and pressure (b) following the injection of $CO_2$ into the power loop (left-hand side figure) or an extraction of $CO_2$ from the power loop (right-hand side figure) for a tank volume equal to the one of the loop

The compressor inlet pressure adapts to the tank pressure level when the initial tank pressure is equal to 82.5 bar, for higher initial pressure levels the equilibrium pressure in the loop achieves slightly lower values (from 84 bar to 89 bar, Figure 5.b). The pressure at the turbine inlet follows the same trend, rising from the nominal value of 132 bar to 139 bar, 145 bar, 149 bar, 152 bar and 156 bar for increasing tank initial pressure levels (82.5 bar, 90 bar, 97.5 bar, 105 bar and 112.5 bar respectively).

Withdrawing $CO_2$ from the circuit, leads to a drop in the $CO_2$ pressure both at inlet to the compressor and turbine (Figure 5.d). It can also be noticed that large amount of fluid withdrawn, introduce small instabilities in lead to undesirable conditions for some system components (i.e. condensation occurring at the compressor inlet, Figures 5.c and 5.d). Further investigations into best locations in the loop for charging/discharging may improve the system pressure response during such transient operating conditions.

### *4.2. Inventory tank volume effect*

The same analysis has been carried out considering different volumes for the inventory tanks. Figure 6.a shows the pressure values achieved in the circuit after $CO_2$ injection/withdrawal considering inventory tanks with a volume (capacity) equal to 30%, 100% and 300% of the total loop one (including the receiver). The equilibrium pressure in the power loop gets closer to the initial pressure of the tank when its capacity increases, since for higher volume of the inventory tanks, the mass injected into the loop is higher. Such higher mass in the circuit also leads to the achievement of lower temperatures at turbine inlet, since the heat input from the waste heat source is kept constant during the simulation. For instance, a turbine inlet temperature equal to 300°C is achieved for a tank volume of 0.729 $m^3$ and an initial pressure of 112.5 bar (Figure 6.b). Similar effects are also noticeable in case of $CO_2$ withdrawal from the power loop.

Higher tank volumes lead to an extended controllability range, e.g. lower temperatures achievable at the turbine inlet, and can ensure a more prolonged availability of the control action (slower tank discharging/charging). On the other hand, larger tank volumes would lead to challenging designs for the inventory tank thermal management system, because of the increased fluid thermal inertia. This is a challenging scenario, since the thermal management of inventory control tanks is among the possible solutions to restore the availability of the inventory controller after use (i.e. providing/removing heat to increase/decrease the tank pressure after usage). The adoption of large inventory tanks would then require auxiliary mechanical systems (i.e. additional pumps, gas booster and valves) to promptly restore the initial tank pressure level.

Figure 7 shows that the same amplifying effects are noticeable on turbine inlet pressure (Figure 7.a) and on the $CO_2$ mass flow rate circulating in the power loop (Figure 7.b). In case of $CO_2$ injection, having a high capacity inventory tank leads to much higher level of mass in the circuit which increases substantially the pressure at inlet of the turbine (maximum level of 180 bar for an inventory tank initial pressure and volume of 112.5 bar and 0.729 $m^3$ respectively). The increased pressure level may overcome pressure design limits of the system, imposing constrains on the maximum mass of fluid injectable in the power loop.

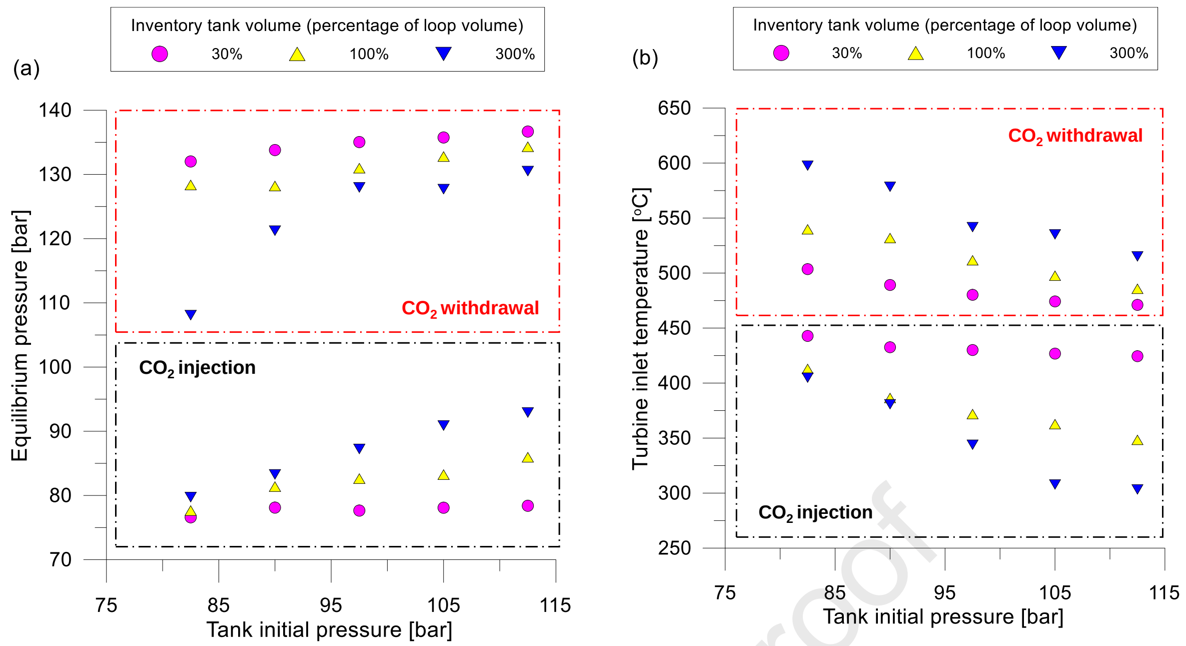


Figure 6 – Effects on system equilibrium pressure (a) and turbine inlet temperature (b) following the injection or withdrawal of fluid into and from the power loop for different inventory tank volumes (expressed as percentage of the loop capacity)

In case of $CO_2$ withdrawal, having a large volume inventory tank (300 % of power loop volume) allows to achieve larger decrease in system pressure level (minimum turbine pressure of 110 bar for a tank initial pressure of 82.5 bar, Figure 7.a) which may be a key feature for the implementation of less complex and more autonomous shutdown control strategies (isolating valves between low and high pressure side of the systems can indeed be avoided since the inventory control system can lower the equalizing cycle pressure in case of compressor shutdown).

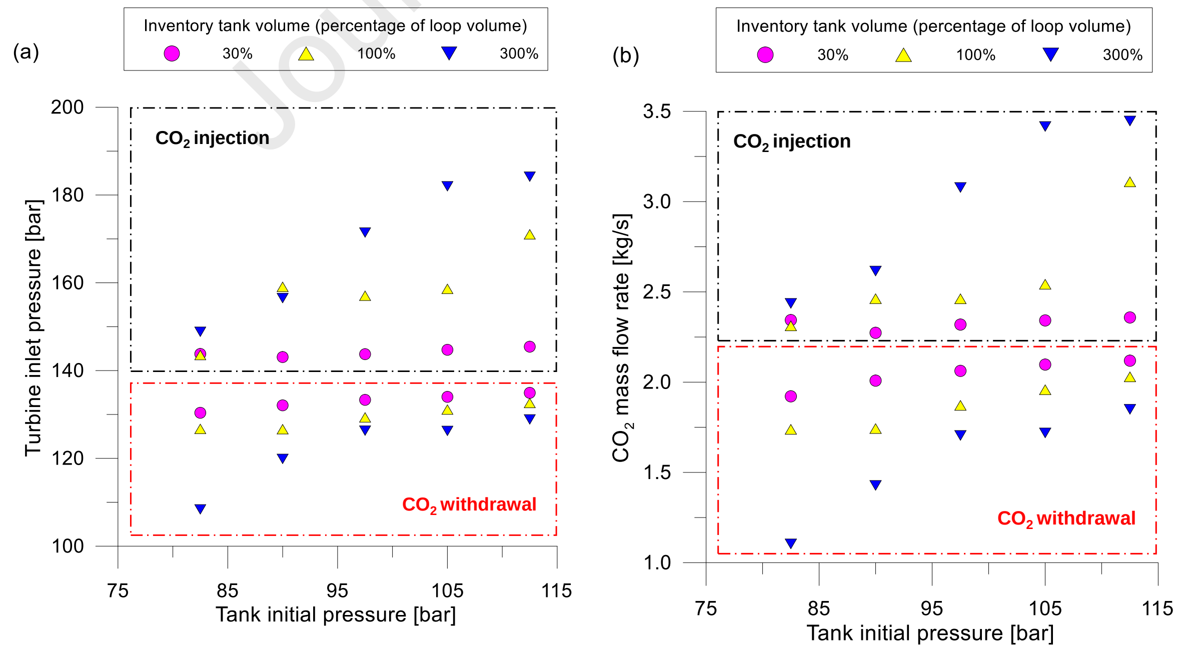


Figure 7 – Turbine inlet pressure (a) and $CO_2$ mass flow rate (b) following the injection or withdrawal of fluid into and from the power loop for different inventory tank volumes (expressed as percentage of the loop capacity)

$CO_2$ injection/withdrawal can substantially increase and decrease respectively the mass flow rate of $CO_2$ circulating in the loop (Figure 7.b), leading to a change also in the pressure drops across heat exchangers.

All the above effects are due to the increased or decreased level of fluid mass in the system, as showed in Figure 8. Figure 8.a shows the additional mass injected to the power loop for different initial pressure levels and inventory tank volumes while Figure 8.b shows the mass removed from the power loop. Increasing the capacity of inventory tank from 100% to 300% of the power loop volume can lead to an increase in injected fluid mass from 9 kg to almost 18 kg for an inventory tank initial pressure of 115 bar (Figure 8.a).

During the extraction, for the same volume increase, the removed mass from the power loop can vary from 19 kg to 31 kg for an initial pressure of the inventory tank of 82.5 bar (Figure 8.b). These results suggest that there is a difference among controllability ranges between $CO_2$ injection and extraction. Assuming same values for the initial pressure levels of both inventory tanks connected to the low- and high-pressure side of the circuit, leads to asymmetric pressure differences between inventory tank and extraction/injection points, with a consequent different effect of the control action. Therefore, inventory sizing should consider this aspect and assume different initial pressure levels for the tanks connected to the low- and high-pressure side of the system.

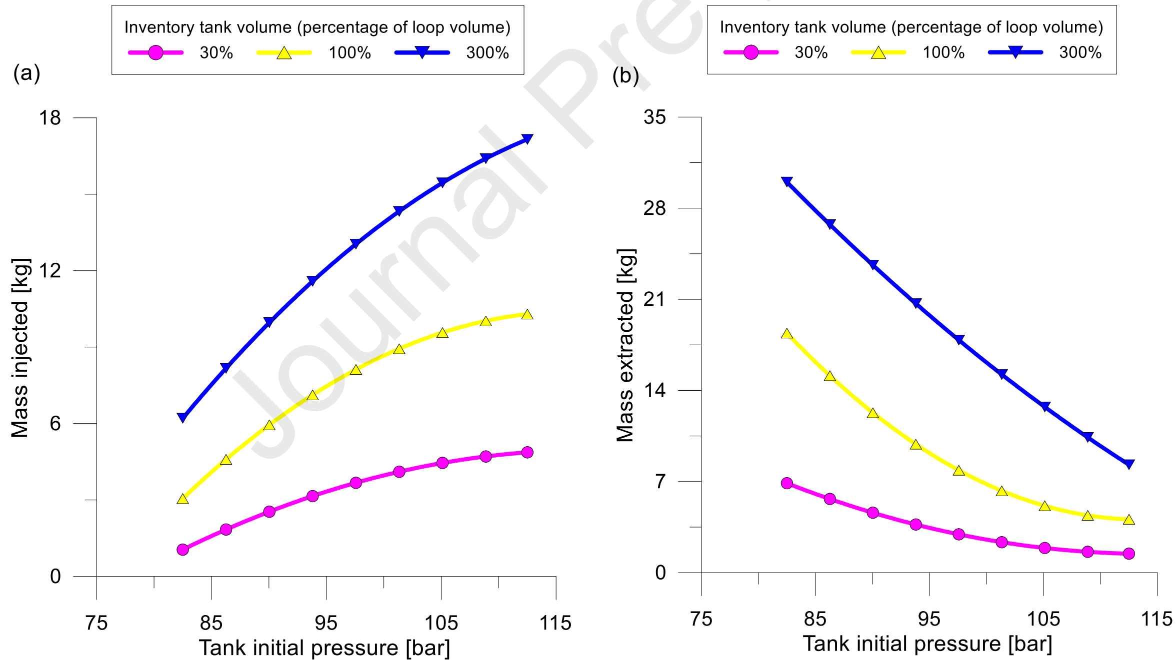


Figure 8 - Compressor inlet temperature as a function of pressure (a) and pressure (b) following the injection of $CO_2$ into the power loop (left-hand side figure) or an extraction of $CO_2$ from the power loop (right-hand side figure) for a tank volume equal to the one of the loop

### *4.3. Inventory effect on system performance*

Figures 9 and 10 show the variation of system performance as a function of initial pressure and volume of the inventory tank following an injection and extraction of fluid. Figure 9 reports the variation of system net power output and Figure 10 the change in cycle efficiency. In particular, Figure 9.a shows the system net power output as the fluid is injected in the power loop. When the volume of the inventory tanks increases the mass injected in the loop for each initial pressure level increases as well, since more working fluid mass transfer is required to equalize the differential pressure between the tanks and the circuit. Small mass injections improve the system power output, because higher mass flow rates are circulating in the circuit. This allows to recover additional thermal power from flue gases without increasing excessively pressure drops across heat exchangers and changing excessively the thermodynamic conditions at turbine and compressor inlet as showed in Figure 6.b, Figure 7.a and Figure 11.a (whose efficiency then remain approximately constant).

Further additions of mass, however, can change significantly the thermodynamic conditions in the cycle and the $CO_2$ mass flow rate, which can impact negatively the efficiency of turbomachinery and the power generated by the power block. Simulation results showed the system power output drops to 77 kW and 66 kW for large amounts of $CO_2$ mass injected, occurring for a tank initial pressure of 112.5 bar and an inventory tank volume of 0.243 $m^3$ and 0.729 $m^3$ respectively (Figure 9.a).

There is then an optimal value of mass injected which maximises the power generated and it is different from the optimal charge that guarantees the system maximum thermal efficiency. Such condition, when the system is slightly overcharged occurs for a volume of the inventory tank equal to 0.243 $m^3$ and an initial pressure level of 97.5 bar (Figure 9.a), corresponding to 8 kg of $CO_2$ mass injected (Figure 8.a).

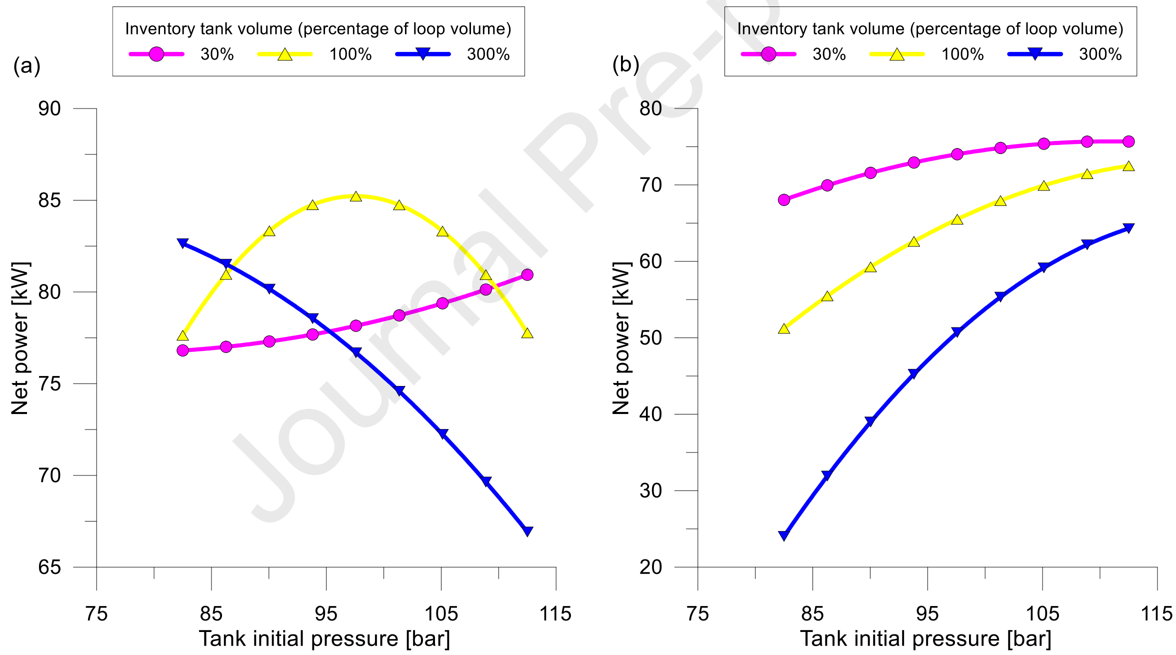


Figure 9 – Net power output of the system as a function of the inventory tank initial pressure level and volume following the injection of $CO_2$ into the power loop (a) or the extraction of $CO_2$ from the power loop (b)

$CO_2$ extraction from the power loop only decreases the system net power output, as shown in Figure 9.b. This is mainly due to the decrease of the turbine inlet pressure and the increase of the temperature at the compressor inlet (as showed in Figure 11.b) which leads to less efficient compression since the machine is operating far from the $CO_2$ critical point.

Similar trends can be observed from the system cycle efficiency results reported in Figure 10, with the only exception occurring during fluid extraction. In Figure 10.b it can be seen that the cycle efficiency slightly improves for small fluid extractions before decreasing substantially for larger removed amounts. Small reductions of fluid mass can lead to steeper drops in the heat recovered rather than on system net power output, causing the efficiency to increase. It can also be seen that the optimal charge for maximum efficiency may be different from the one required to achieve maximum power output.

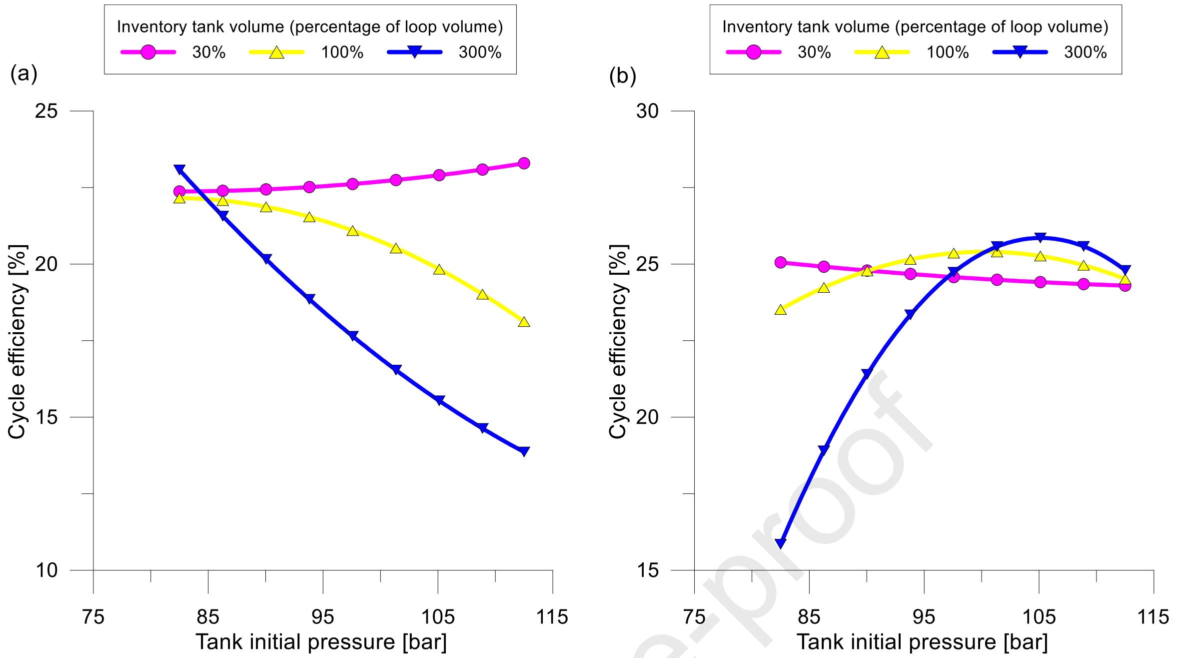


Figure 10 – Cycle efficiency of the system as a function of the inventory tank initial pressure level and volume following the injection of $CO_2$ into the power loop (a) or the extraction of $CO_2$ from the power loop (b)

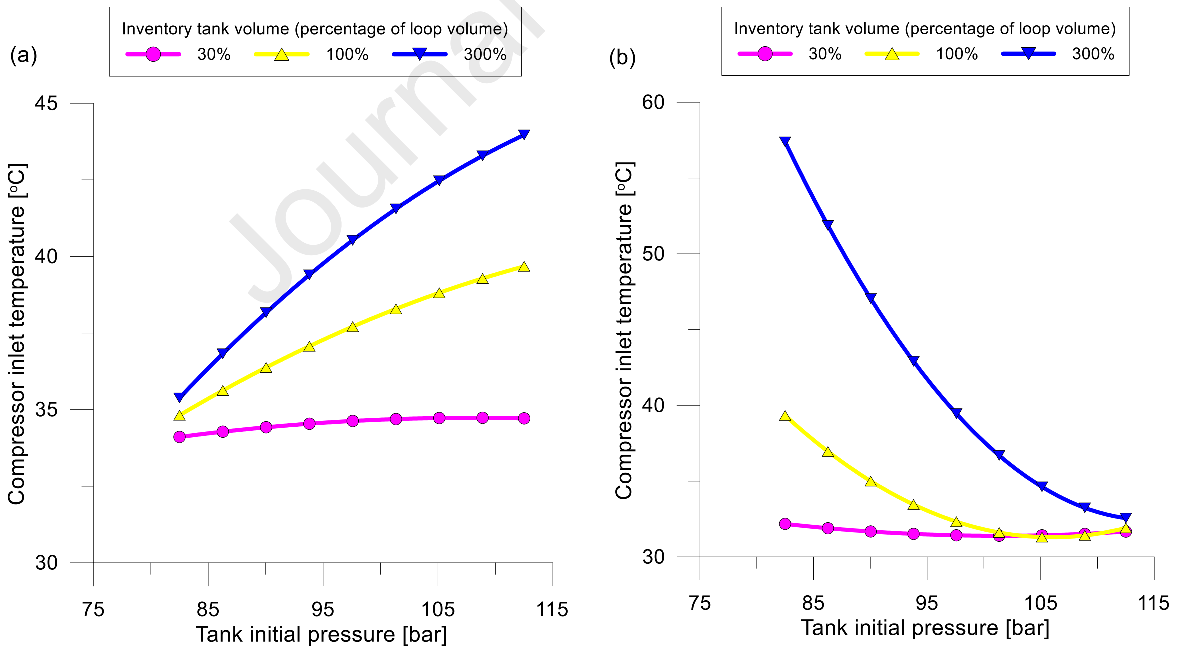


Figure 11 - Compressor inlet temperature as a function of pressure (a) and pressure (b) following the injection of $CO_2$ into the power loop (left-hand side figure) or an extraction of $CO_2$ from the power loop (right-hand side figure) for a tank volume equal to the one of the loop

## 5. Inventory control simulations

After the analysis of the effects of inventory main parameters on system variables and performance, an inventory controller was designed to regulate the temperature at the turbine inlet. The temperature at the inlet of the turbine is a crucial parameter to avoid critical thermal stresses on system components and ensure a safe operation of the system and turbomachine auxiliaries (i.e. sealing, bearings) during transients. Because the $sCO_2$ facility has been designed for waste heat recovery applications, the objective is to assess the controller response to a heat load variation. In this study in particular, the case of a heat load drop and increase have been simulated by considering a decrease and increase respectively of the flue gas inlet temperature.

The controller is a Proportional Integral (PI) one acting on the valve actuator lift position. Two such controllers have been connected to the inventory extraction and injection valves (EXTV and INJV respectively, Figure 3). The controller on the EXTV, which connects one inventory tank to the high-pressure side of the power loop (downstream the compressor, point 2 in Figure 3), is activated by a state machine controller when the primary heater sees a decrease in the heat load provided by the flue gases (which may occur for a temperature or flow rate decrease). In such case, fluid mass is removed from the power loop to counterbalance the decrease in thermal energy available.

On the contrary, the controller on the INJV, which connects the other inventory tank to the low-pressure side of the power loop (upstream the compressor, point 1 in Figure 3), is activated by the state machine following a rise in heat source temperature or mass flow rate. Higher thermal energy is therefore balanced by an increase in the mass of fluid in the power loop. The state machine is thus regulated depending on the difference between the actual and the nominal level of temperature or mass flow rate of the heat source. If the difference is positive, means that the heat load provided by the flue gas is higher and then the controller acting on the INJV is activated. If the difference is negative, the controller on the EXTV is used.

A lambda tuning procedure has been used to calculate the proportional (P) and integral (I) terms of the controllers [32]. By considering a first order relationship between the mass injected/extracted into/from the power loop and the controlled process variable (turbine inlet temperature), the control output (valve actuator lift) has been modified in the entire admissible range and the process variable response analysed. From the time constant ($\tau$) and process gain (K), the proportional and integral coefficients of the two controllers have been retrieved by setting an appropriate settling time and damping ratio to smooth the controller response. Table 8 reports PI values for the two controllers with the respective settling time and damping ratio. In the following sections the controller performance and response are discussed in relation to a simulated decrease and increase of the heat load.

Table 8 – Proportional (P) and integral (I) coefficients for controllers acting on the extraction valve (EXTV) and the injection valve (INJV)

| Controller coefficients | | EXTV | INJV |
|---|---|---|---|
| P coefficient | [-] | 0.31 | -0.37 |
| I coefficient | [-] | 0.09 | -0.07 |
| Settling time | [s] | 21 | |
| Damping ratio | [-] | 0.8 | |

### 5.1. *Heat load decrease*

Figure 12 shows the results of the system uncontrolled and controlled responses to a decrease in the heat load provided by the waste heat source, simulated through a decrease of 10% in the inlet temperature, form 650 °C down to 580 °C (grey continuous line, Figure 12.a). The temperature control set point (dashed red line in Figure 12.a) at the turbine inlet has been set equal to the turbine nominal temperature of 465 °C. The inventory tank volume was assumed equal to 0.243 $m^3$ (same for the power loop), while its initial pressure has been set to 82.5 bar. Without control action, the turbine inlet temperature decreases from 465 °C to 400 °C, leading to a 65 °C temperature drop in approximately 50s. Turbine pressure, compressor inlet conditions, and mass flow rate remain on the contrary unchanged (Figure 12.a, 12.c and 12.d). Once the inventory control system is active, the regulation of the turbine temperatures is effective and the reference set point is achieved thanks to the removal of 11 kg of fluid mass from the power loop (dark brown continuous line in Figure 12.b).

As a result of the mass removal, the turbine and compressor inlet pressures decrease from the nominal value of 137.5 bar and 75 bar down to 126 bar and 72 bar respectively (blue and light brown line respectively in Figure 12.c). The mass flow rate also decreases from the nominal value of 2.2 kg/s down to 1.8 kg/s (pastel blue line in Figure 12.d). This is a consequence of the reduced pressure ratio across the cycle induced by the lower fluid mass in the circuit, which changes the characteristic of the loop and reduces the mass flow provided by the compressor.

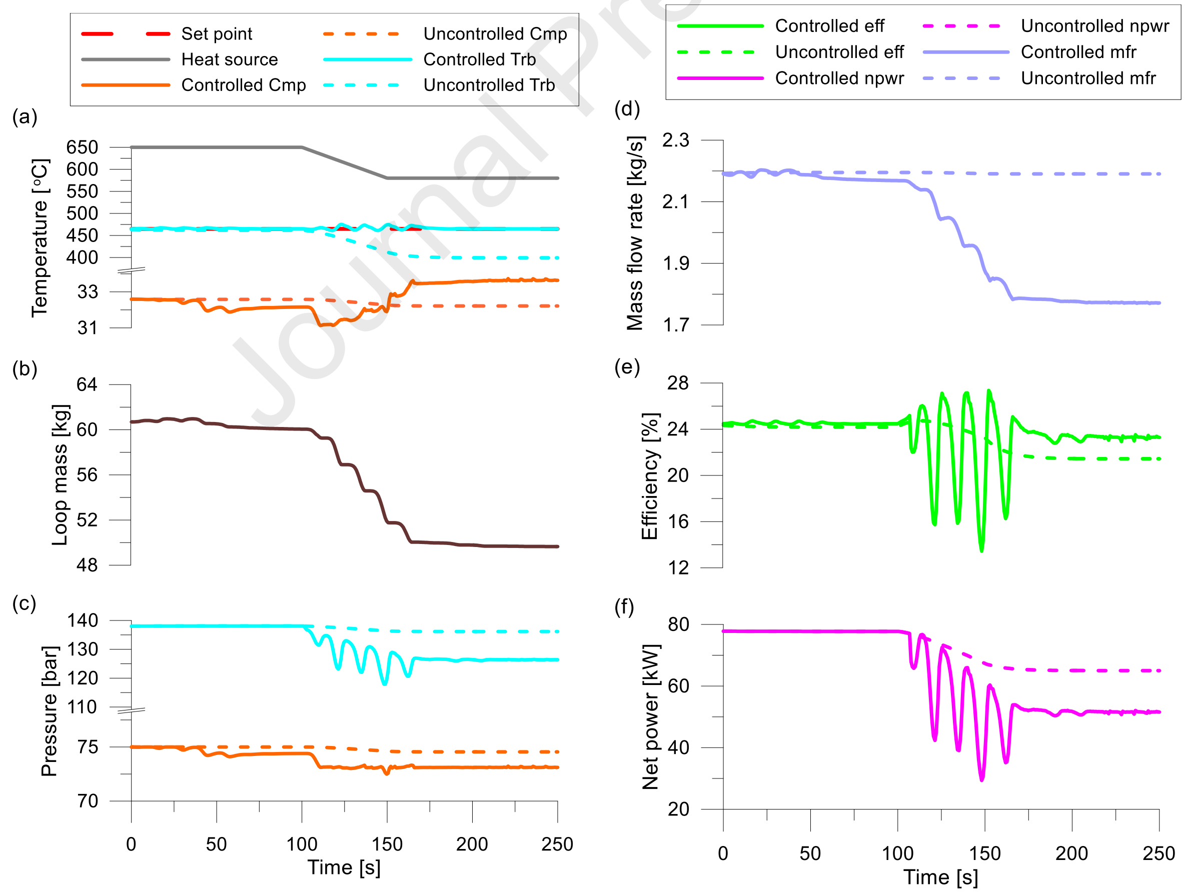


Figure 12 – Controlled and uncontrolled system response to a decrease in the heat source (hs) temperature: (a) set point, compressor (cmp) and turbine (trb) inlet temperatures; (b) mass in the power loop; (c) compressor and turbine inlet pressures; (d) $CO_2$ mass flow rate (mfr); (e) cycle efficiency (eff); (f) net power output (npwr)

The removal of $CO_2$ from the power loop causes the compressor to operate close to the surge region, with oscillations at the outlet pressure which consequently result in oscillation in all the cycle calculated quantities, from the mass flow rate to the efficiency and net power output. More detailed analyses of the compressor operations (both numerical and experimental) would be required in future work to understand if an anti-surge valve can help to overcome the issue.

Figure 12.e and Figure 12.f show the effect of the inventory control action on the system performance. In particular the cycle efficiency is showed in Figure 12.e while the system net power output in Figure 12.f. The decrease in heat load has a detrimental effect on both efficiency and net power output. When the control system is not considered the efficiency of the cycle drops from 24% down to 22% (dark green line in Figure 12.e) following a decrease in the heat source temperature. The thermal power recovered from the flue gases stays the same, but the net power decreases from 78 kW to 65 kW (purple line in Figure 12.f).

The action of the inventory controller despite leading to a lower net power output of 52 kW (magenta line in Figure 12.f), 20% lower compared to the uncontrolled system, allows to achieve a higher cycle efficiency after the heat source temperature decrease (light green line in Figure 12.e). The less mass of fluid in the power loop indeed leads to a lower power production, but also to a much lower waste heat recovered compared to the uncontrolled system case, allowing to maintain a constant efficiency in part load conditions. Such results suggest that inventory control strategies for regulating the power unit in part-load conditions should be preferred in power generation applications rather than waste heat recovery, where the net power generated has a higher value (since the heat source is a waste product).

### *5.2. Heat load increase*

Figure 13 shows system uncontrolled and controlled response for an increase of the heat load provided by the flue gases, simulated through an increase of 10% in the inlet temperature, which goes from the nominal value of 650°C up to 725°C (grey continuous line, Figure 13.a). In this case as well the temperature control set point has been kept equal to the turbine nominal temperature of 465°C (Figure 13.a). The inventory initial pressure to 112.5 bar while the volume of the inventory tank has been set equal to 0.729 $m^3$. Simulations adopting a volume of 0.243 $m^3$, in fact, revealed the inability of the controller to achieve the target due to the saturation of control action. The available mass before the equalization of pressure between tank and power loop was not sufficient to cause an adequate drop in turbine inlet temperature.

When the system is not controlled, the turbine inlet temperature increases from 465°C to 532°C, leading also in this case to approximately 65°C temperature difference in 50s. The pressure at the turbine and compressor inlet along with the compressor inlet temperature and $CO_2$ mass flow rate remains unchanged (Figure 13.a, 13.c and 13.d). The inventory controller instead even in this case is able to keep the turbine inlet temperature equal to the established set point (blue line in Figure 13.a) by adding 7 kg of fluid mass into the power loop (dark brown line in Figure 13.b). After the injection of the additional fluid mass, the pressure at turbine and compressor inlet increase from the nominal value of 137.5 bar and 75 bar up to 155 bar and 82 bar respectively (blue and light brown line respectively in Figure 13.c). The mass flow rate increases as well from the nominal value of 2.2 kg/s up to 2.5 kg/s (pastel line in Figure 13.d) following the increased cycle pressure ratio.

In this case, the inventory controller actually allows not only to promptly regulate the system but also to achieve better performance in terms of net power output, which goes from 77 kW up to 92 kW against the increase from 77 kW to 88 kW obtained in the uncontrolled case (Figure 13.f). In terms of cycle efficiency, Figure 13.e shows that for an increase in the heat load the inventory controller allows to keep the system efficiency unchanged but lower compared to the one achieved by the uncontrolled power unit 26% when the waste heat source temperature achieves 725°C (dark green light in Figure 13.e). Such results show that for increases of heat load provided by the waste heat source, the inventory controller is actually very effective also in optimizing system performance. Either in this case oscillating transients can be noticed due to the particular region of operation of the compressor.

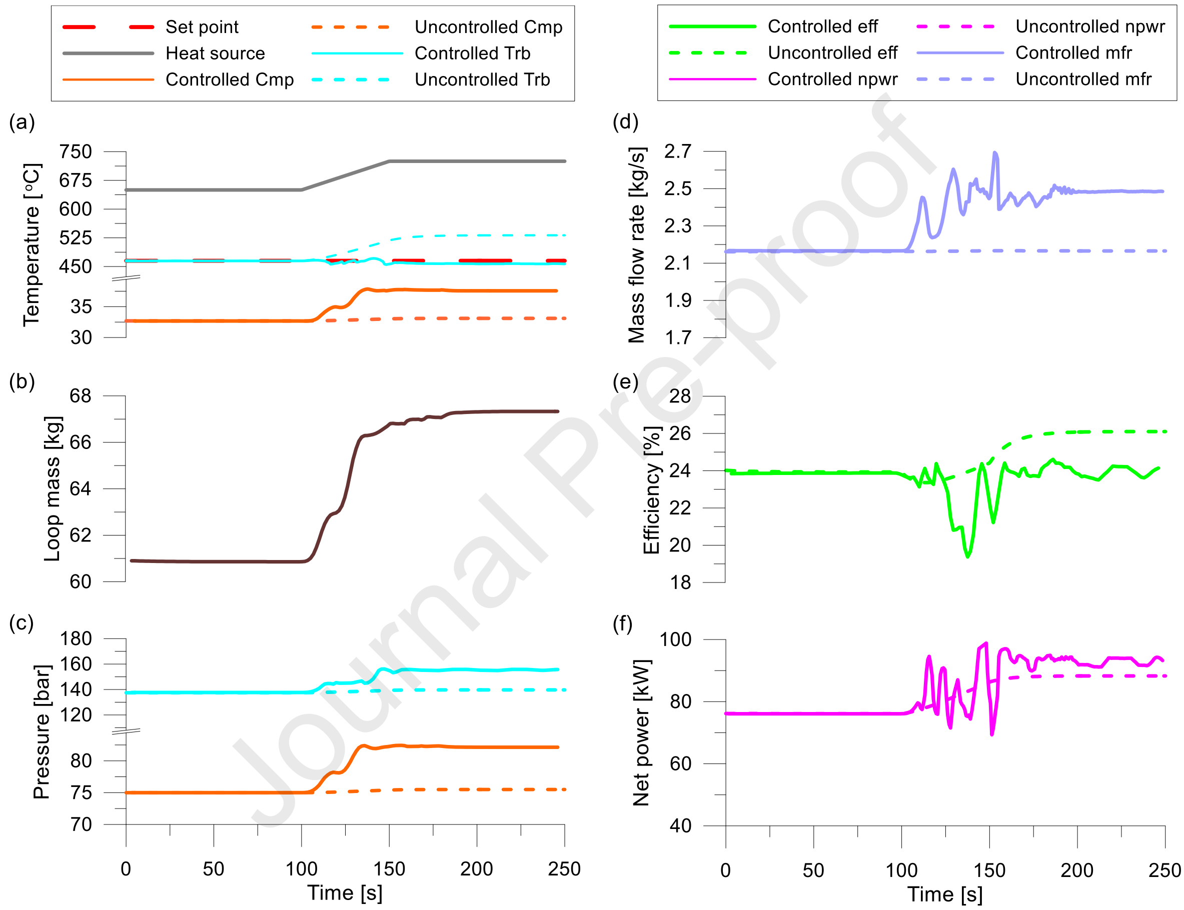


Figure 13 – Controlled and uncontrolled system response to an increase in the heat source (hs) temperature: (a) set point, compressor (cmp) and turbine (trb) inlet temperatures; (b) mass in the power loop; (c) compressor and turbine inlet pressures; (d) $CO_2$ mass flow rate (mfr); (e) cycle efficiency (eff); (f) net power output (npwr)

## 6. Conclusions

This work provides insights on the dynamics of inventory control on a small scale $sCO_2$ heat to power conversion unit. The numerical methodology combines a one-dimensional CFD model of the $sCO_2$ power loop calibrated against real equipment data with a model of an inventory control system. The results show that, with respect to inventory design procedures available in the literature, the sizing of the inventory tanks cannot be carried out assuming $CO_2$ injection and withdrawal processes are isothermal. The simulations reported a maximum tank temperature change of 22% and 76% when the $CO_2$ is injected and withdrawn from the system respectively.

Such temperature change could lead to variation of fluid thermophysical properties with consequent errors in the prediction of the control action outcomes. As inventory tank capacity is mainly related to the controllability range of the cycle, increasing the volume to 3 times that of the power loop led to ±30% variation in turbine inlet temperature compared to the nominal value. Larger tank volume could also lead to greater control flexibility but also to increased complexity in inventory thermal management, potentially requiring the use of mechanical systems (i.e. pumps, gas boosters, valves or multiple tanks) to restore the initial tank pressure level and therefore the control margin after multiple fluid injections/withdrawals to and from the power loop.

In general, even if the inventory controller can effectively regulate the turbine inlet temperature by injecting/withdrawing $CO_2$ into/from the power loop, such action influences several cycle parameters, with consequent complexity in predicting the outcome on system performance. For example, a decrease of 10% in the waste heat source temperature, the extraction of 11 kg of $CO_2$ mass from the power loop enacted by the PI inventory controller enables the turbine inlet temperature to remain constant at the nominal value of 465°C but causes a 11 bar and a 2 bar reduction in the turbine and compressor inlet pressures respectively.

This combined with a decrease in $CO_2$ mass flow rate of 0.4 kg/s leads to a reduction in net power output of 13 kW but to an increase in efficiency of 2% compared to the performance of the uncontrolled system. Therefore, despite a small detrimental action on the power output, at part-load the controller is able to keep unchanged the cycle efficiency when the heat source temperature decreases. For a heat source temperature increase the controller is able to optimise the system net power output while keeping a constant cycle efficiency. Future work will be focused on assessing the relationship between mass injected/extracted and cycle performance as well as identifying strategies to improve transients occurring during the actuation of the control action.



**Acknowledgement**

The research presented in this paper has received funding from the European Union’s Horizon 2020 research and innovation program under grant agreement No. 680599 for the I-ThERM project. Funding for the work has also been received from the Research Councils UK, Grant No. EP/P004636 for the OPTEMIN project and Grant No, EP/V001795/1 for the SCOTWAHR project. The contribution from the funders and industry partners in these projects is gratefully acknowledged. Data related to the paper and other information relating to the paper can be obtained by contacting the corresponding author.

**References**

[1] White MT, Bianchi G, Chai L, Tassou SA, Sayma AI. Review of supercritical $CO_2$ technologies and systems for power generation. Applied Thermal Engineering 2021;185. doi.org/10.1016/j.applthermaleng.2020.116447.

[2] Marchionni M, Bianchi G, Tassou SA. Review of supercritical carbon dioxide ($sCO_2$) technologies for high-grade waste heat to power conversion. SN Applied Sciences 2020;2: 611. doi.org/10.1007/s42452-020-2116-6.

[3] Li H, Ju Y, Zhang C. Optimization of supercritical carbon dioxide recompression Brayton cycle considering anti-condensation design of centrifugal compressor. Fuel 2016;180:694-717. doi.org/10.1016/j.enconman.2022.115207.

[4] Crespi F, Rodríguez de Arriba P, Sánchez D, Ayub A, Di Marcoberardino G, Invernizzi CM, Martínez GS, Iora P, Di Bona D, Binotti M, Manzolini G. Thermal efficiency gains enabled by using $CO_2$ mixtures in supercritical power cycles. Energy 2022;238:121899. doi.org/10.1016/j.energy.2021.121899.

[5] Olumayegun O, Meihong W, Greg K. Closed-cycle gas turbine for power generation: A state-of-the-art review. Energy Conversion and Management 2022;254:115207. doi.org/10.1016/j.fuel.2016.04.074.

[6] Wright SA, Radel RF, Vernon ME, Rochau GE, Pickard PS. SANDIA REPORT. Operation and Analysis of a Supercritical $CO_2$ Brayton Cycle. 2012.

[7] Luu MT, Milani D, McNaughton R, Abbas A. Advanced control strategies for dynamic operation of a solar-assisted recompression supercritical $CO_2$ Brayton power cycle. Applied Thermal Engineering 2018;136:682–700. doi.org/10.1016/j.applthermaleng.2018.03.021.

[8] Clementoni EM, Cox TL, King MA, Rahner KD. Transient Power Operation of a Supercritical Carbon Dioxide Brayton Cycle. 2017.

[9] Moisseytsev A, Kulesza KP, Sienicki JJ. Control System Options and Strategies for Supercritical $CO_2$ Cycles. 2009. doi.org/https://doi.org/10.2172/958037.

[10] Heifetz A, Vilim R. Turbine bypass, mass inventory, and mixed-mode generator power control of S-$CO_2$ recompression cycle. Nuclear Technology 2015;189:268–77. doi.org/10.13182/NT13-113.

[11] Oh BS, Jeong Y, Cho SK, Lee JI. Controllability of S-$CO_2$ power system coupled small modular reactor with improved compressor design. Applied Thermal Engineering 2021;192:116957. doi.org/10.1016/j.applthermaleng.2021.116957.

[12] Reay DA. Compact heat exchangers: A review of current equipment and R&D in the field. Heat Recovery Systems and CHP 1994;14:459–74. doi.org/10.1016/0890-4332(94)90050-7.

[13] Jiang Y, Liese E, Zitney SE, Bhattacharyya D. Design and dynamic modeling of printed circuit heat exchangers for supercritical carbon dioxide Brayton power cycles. Applied Energy 2018;231:1019–32. doi.org/10.1016/j.apenergy.2018.09.193.

[14] Park JH, Kwon JG, Kim TH, Kim MH, Cha JE, Jo HJ. Experimental study of a straight channel printed circuit heat exchanger on supercritical $CO_2$ near the critical point with water cooling. International Journal of Heat and Mass Transfer 2020;150:119364. doi.org/10.1016/j.ijheatmasstransfer.2020.119364.

[15] Marchionni M, Bianchi G, Tassou SA. Techno-economic assessment of Joule-Brayton cycle architectures for heat to power conversion from high-grade heat sources using $CO_2$ in the supercritical state. Energy 2018;148:1140–52. doi.org/10.1016/J.ENERGY.2018.02.005.

[16] Shiferaw D, Carrero J, Pierres RL. Economic analysis of $SCO_2$ cycles with PCHE Recuperator design optimisation, 2016.

[17] Fuller R, Preuss J, Noall J. Turbomachinery for supercritical $CO_2$ power cycles. Proceedings of the ASME Turbo Expo, vol. 5, American Society of Mechanical Engineers Digital Collection; 2012, p. 961–6. doi.org/10.1115/GT2012-68735.

[18] Bianchi G, Saravi SS, Loeb R, Tsamos KM, Marchionni M, Leroux A. Design of a high-temperature heat to power conversion facility for testing supercritical $CO_2$ equipment and packaged power units. Energy Procedia 2019;161:421–8. https://doi.org/10.1016/J.EGYPRO.2019.02.109.

[19] T Gamma - Gamma Technologies Inc 2020. GT-SUITE-Flow Theory Manual 2020.

[20] Gnielinski V. New equation for heat and mass transfer in turbulent pipe and channel flow. International Chemical Engineering 1976;16:359–68.

[21] Dittus FW, Boelter LMK. Heat transfer in automobile radiators of the tubular type. International Communications in Heat and Mass Transfer 1985;12:3–22. doi.org/10.1016/0735-1933(85)90003-X.

[22] Marchionni M, Chai L, Bianchi G, Tassou SA. Numerical modelling and transient analysis of a printed circuit heat exchanger used as recuperator for supercritical $CO_2$ heat to power conversion systems. Applied Thermal Engineering 2019;161:114190. doi.org/10.1016/j.applthermaleng.2019.114190.

[23] Brkić D. Review of explicit approximations to the Colebrook relation for flow friction. Journal of Petroleum Science and Engineering 2011;77:34–48. doi.org/10.1016/J.PETROL.2011.02.006.

[24] Prosperetti A. A generalization of the Rayleigh–Plesset equation of bubble dynamics. Physics of Fluids 1982;25:409. doi.org/10.1063/1.863775.

[25] Marchionni M, Bianchi G, Karvountzis-Kontakiotis A, Pesyridis A, Tassou SA. An appraisal of proportional integral control strategies for small scale waste heat to power conversion units based on Organic Rankine Cycles. Energy 2018;163:1062–76. doi.org/10.1016/J.ENERGY.2018.08.156.

[26] Saravi SS. An investigation into $sCO_2$ compressor performance prediction in the supercritical region for power systems. Energy Procedia 2019;161:403–11. doi.org/10.1016/J.EGYPRO.2019.02.098.

[27] Marchionni M, Saravi SS, Bianchi G, Tassou SA. Modelling and performance analysis of a supercritical $CO_2$ system for high temperature industrial heat to power conversion at off-design conditions. 3rd European $sCO_2$ conference, 2019. doi.org/10.17185/duepublico/48908.

[28] Wright SA, Radel RF, Vernon ME, Rochau GE, Pickard PS. Operation and Analysis of a Supercritical $CO_2$ Brayton Cycle. 2010. doi.org/10.2172/984129.

[29] Dyreby JJ, Klein SA, Nellis GF, Reindl DT. Modeling Off-Design and Part-Load Performance of Supercritical Carbon Dioxide Power Cycles. 2013.

[30] Samson. Type 3252 High-pressure Valve, [online], https://www.samsoncontrols.net/heavydutyindustrialapplication2.html

[31] Lemmon EW, Huber ML, Mclinden MO. NIST Standard Reference Database 23: Reference Fluid Thermodynamic and Transport Properties-REFPROP, Version 9.1, Natl Std. Ref. Data Series (NIST NSRDS), National Institute of Standards and Technology, Gaithersburg, MD, [online], https://tsapps.nist.gov/publication/get_pdf.cfm?pub_id=912382

[32] Lennartson B, Kristiansson B. Evaluation and tuning of robust PID controllers. IET Control Theory Application 2009;3:294–302. doi:10.1049/iet-cta:20060450.

**Declaration of interests**

☒ The authors declare that they have no known competing financial interests or personal relationships that could have appeared to influence the work reported in this paper.

☐The authors declare the following financial interests/personal relationships which may be considered as potential competing interests: